Surface temperature measurement of acoustic liners in presence of grazing flow and thermal gradient

Victor Lafont, Fabien Méry, Philippe Reulet, Frank Simon

Surface temperature measurement of acoustic liners in presence of grazing flow and thermal gradient

Victor Lafont · Fabien Méry · Philippe Reulet · Frank Simon

February 3, 2021

Abstract The development of turbofans with larger fan diameters, shorter inlets, and thinner walls forces the acoustic liners to be placed closer to the hot parts of engines. This experimental study investigates the combined effects of large thermal gradients, grazing flow and acoustic level on the impedance of liners. Previous studies have shown that a coupling between these three effects can exist. The objective is thus to understand the underlying coupled phenomena, in order to extract the driving parameters for a more accurate impedance modelling.
In the ONERA B2A grazing flow acoustic liner facility, the flow temperature can be accurately regulated and several types of acoustic excitation can be provided. For the purposes of this study, a test section with a heating device is used to obtain a thermal gradient between the backplate and the perforated plate of the liner sample.
Infrared (IR) thermography is used to measure the temperature distribution on the perforated plate. The measurement is conducted for several configurations, to determine in which conditions the coupling between thermal and acoustic dissipation effects exists. In particular, a possible control of surface temperature by high sound pressure level is highlighted.

Keywords Acoustic liner · Thermal effect · Infrared thermography · Liner impedance eduction

Nomenclature

M_b	Grazing flow bulk Mach number
S	B2A cross section area (mm^2)
α	Liner absorption coefficient
δ	Liner perforated sheet thickness (mm)
ω	Angular frequency (rad/s)
ϕ	Liner perforated sheet hole diameter (mm)
ρ_0	Density of the mean flow (kg/m^3)
a	B2A cross section height (mm)
c_0	Speed of sound in air (m/s)
q_m	Mass flow rate (g/s)
(x, y, z)	Axial, transverse and vertical coordinates
ζ	Normalized acoustic impedance
χ	Normalized acoustic reactance (imaginary part of ζ)
r	Normalized acoustic resistance (real part of ζ)
SPL	Sound Pressure Level (dB)
P_d	Power transmitted on the backplate (W/m^2)
T_b	Backplate temperature (°C)
T_{flow}	Grazing flow static temperature (°C)
T_{lat}	Lateral temperature (°C)
T_u	Perforated plate adiabatic temperature (°C)
Bi	Biot number
h	Convective heat transfer coefficient (W/m^2/K)
k_{al}	Aluminum thermal conductivity (W/m/K)
k_{body}	Sample thermal conductivity (W/m/K)

ONERA/DMPE, Université de Toulouse, 2 avenue Edouard Belin, 31055 Toulouse, France
E-mail: victor.lafont@onera.fr E-mail: fabien.mery@onera.fr

1 Introduction

Future UHBR (Ultra High Bypass Ratio) engines will be designed for maximum propulsion efficiency. To achieve these optimum conditions, nacelles will have to be lighter, with thinner walls, shorter inlets and outlets, and a larger fan diameter. With these changes, new challenges arise regarding the implementation of conventional noise-absorbing liners: thinner and shorter nacelles imply less room to accommodate acoustic liners while their height needs to be increased in order to properly absorb the lower-frequency noise created by a larger fan. Moreover, the shorter inlets

and thinner walls between the combustion chamber and the bypass ducts favor the apparition of thermal gradients inside the liners' structure itself. Therefore, there is a need to characterize as comprehensively as possible the behavior of conventional acoustic liners when thermal gradients, complex flows and high noise levels are all involved.

Conventional single degree of freedom (SDOF) liners consist of a honeycomb structure topped with a perforated facesheet and closed by a rigid backplate, forming a layout of small resonators. The geometry of the honeycomb can be adjusted to match specific noise damping requirements (Motsinger and Kraft 1991). The driving parameter for the noise damping power of liners is their acoustic impedance, i.e. the ratio between acoustic pressure and normal acoustic velocity taken on the facesheet normalized by $\rho_0 c_0$.

$$\zeta(\omega) = \frac{Z(\omega)}{\rho_0 c_0} = \frac{p}{\rho_0 c_0 v_n}$$

The impedance ζ is a complex number, its real part r and imaginary part χ are respectively called the resistance and the reactance of the liner.

The value of the impedance can be experimentally determined with several methods. Direct approaches, such as the standing-wave method using an impedance tube, the two-microphone method and the in-situ method, are commonly used to measure the normal incidence impedance (Chung and Blaser 1980; Bodén and Åbom 1986).

These methods rely on the equations governing acoustic propagation in ducts and cavities and are easy to implement in no-flow cases. However they are often not suited to measurements in presence of grazing flow due to strong near field effects.

These problems motivated the development of indirect approaches, which rely on matching the measured acoustic field and a modeled acoustic field through a minimization method, the parameter being the impedance of the liner (Elnady and Bodén 2004; Elnady et al. 2009; Busse-Gerstengarbe et al. 2012; Lavieille et al. 2006) or the axial wavenumbers which can be straightforwardly linked to the impedance when a uniform flow hypothesis is taken (Jing et al. 2008). First developments of these indirect methods were conducted by NASA (Watson et al. 1996, 1999; Jones et al. 2005), where microphones probes were placed in the wall opposite the liner and a finite element method was used to solve the convected Helmholtz equations (CHE) in order to find the liner impedance. Elnady and Bodén (2004) used similar pressure measurements and a mode-matching method to educe the impedance, allowing to solve for higher-order acoustic modes.

In order to get information closer to the liner than with microphone measurements located on the wall opposite the liner, ONERA used a LDV technique to measure the 2 components of the acoustic velocity fields in the area above the liner, and used them as inputs for the eduction process (Primus et al. 2013; Roncen et al. 2019).

The coupling between aerodynamic and acoustic effects is complex, as liners increase the viscous drag in the turbulent layer compared to a smooth surface. Howerton and Jones (2017) investigated the drag effect of several conventional or more advanced liner designs in the NASA GFIT. They found that the resistance factor (or friction factor) λ was frequency-dependent in presence of acoustic excitation. This dependence increased with sound pressure level (SPL), but was mitigated by higher flow speeds. Jasinski and Corke (0) used hot-wire boundary layer measurements and found that the localized disturbances caused by high acoustic excitations could interact with the wall streak structure when they had a similar scale , thus creating turbulent bursts and increasing the viscous drag. Zhang and Bodony (2016) performed a series of Direct Numerical Simulations reproducing the conditions of a single orifice-over-cavity liner undergoing a grazing flow, and confirmed that high acoustic levels increased the liner drag. Léon et al. (2019) used a high-magnification PIV setup to obtain 2D acoustic velocity fields measured close to the perforations of a SDOF liner sample. They found that near-orifice dynamics depended greatly on the frequency of the acoustic excitation, with different effects near or away from the sample's resonance. They also observed that high acoustic levels induced specific aerodynamic phenomena: in these conditions, a "rough-wall" analysis was showing its limits to predict the effects. However, little is known on the effects of thermal gradients inside or around liners, as most temperature studies on perforated walls have been conducted in the context of combustion chambers. Regarding conventional SDOF liners, only a few studies exist. Elnady et al. (2004) investigated the acoustic behavior of a single orifice over a cavity placed in an oven. The surface of the sample was hotter than the back of the cavity, with a difference of up to 100 K. The measures were conducted at several sound pressure levels (SPL), including levels at which the liner enters non-linear acoustic regime, but without any grazing flow. The impedance of the liner was measured with an in-situ technique and compared to existing semi-empirical models. It was found that an increase in temperature results in a decrease of the reactance, while the resistance slightly increases (at least when the nonlinear effects are small compared to the viscous ones). Modifying the properties of air in the model to account for the high temperatures appeared to be enough to predict quite well this impedance change, as the decrease of the reactance is due to the modification of the air density (and thus the sound velocity) inside the cavity. Rademaker et al. (2009) confirmed this effect on the reactance and found that the effect of temperature on the resistance was weak when compared to the effect of grazing flow. Rademaker also showed that in presence of a hot grazing flow, the temperature was lower inside

the cavity. Méry et al. (2019) conducted a study on liner samples heated from below, both with and without the presence of a cooler grazing flow. The acoustic response of the samples was investigated both in the linear and non-linear regimes with respect to the acoustic level. They showed that the temperature changes mainly impacted the reactance as the sound speed inside the cavities was modified. They also highlighted the influence of the acoustic level on the temperature repartition: at high SPL, the temperature went down inside the cavity due to the sample entering the non-linear regime. This highlighted strong multiphysics coupling between acoustics, flow and thermal phenomena.

In this study, a specific experimental setup is designed and used to monitor the evolution of a classic liner surface temperature when there is a thermal gradient inside it and in presence of high SPL. The measurements are conducted with a cool grazing flow and the experimental conditions are carefully controlled. In particular, the temperature is monitored in several places all along the measurement. The goal is to exhibit the links between the acoustical effects and the aerothermal effects on liner impedance, using the specific eduction technique developed in Lafont et al. (2020).

Section 2 describes our experimental setup, Section 3 focuses on the infrared thermography technique, then the measurements and results are presented in Section 4. Section 5 summarizes the conclusions of this work.

2 Experimental methods and setup

2.1 Sample description

Two different SDOF liner samples are used in this study. Details can be found in Table 1. They have very similar geometries, differing only by the thickness of the perforated sheet. These two liner samples have already been partially characterized with an impedance tube and on the B2A bench (Méry et al. 2019). The main difference between them is their behavior with respect to the sound pressure level (SPL).

Indeed, Hersh et al. (2003) proposed a model to take into account the effect of SPL on the resistance term of the impedance regarding the diameter of the holes and the plate thickness. More recently, Chandrasekharan et al. (2006) led impedance measurements in a tube and compared results with classical laws. It is shown that an increase of the ratio between the plate thickness and the hole radius increases the frequency band over which there is a linear behavior of the liner with the sound level: the impedance is not modified by the SPL. Higher acoustic levels (such as the ones present in aeronautic applications) induce non-linear effects as the high incident sound pressure creates vortex shedding around the openings of the liner surface (Guess 1975; Kirby and Cummings 1998; Rienstra and Singh 2018). As a result, the resistance r increases. Similarly, the presence of a grazing flow generally results in an increase of the resistance (Guess 1975; Kirby and Cummings 1998).

According to these impedance models, SDOF-1 can be considered as non-linear and SDOF-2 as linear regarding the SPL (in the range studied) . The different facesheet thicknesses are 1 and 8 mm, respectively. The other geometric dimensions like perforation and cell cross section are the same. By keeping the total liner height constant this yields a cell height of 48 and 41 mm respectively. The modification of the cavity depth implies a modification of the liner resonance frequency (i.e. maximum absorption under normal acoustic incidence, where the reactance is null) . SDOF-1 has a resonance frequency around 1500 Hz and SDOF-2 has a resonance frequency around 1000 Hz.

Sample SDOF-1 has previously been tested in presence of thermal gradients in Méry et al. (2019). The study concluded that the main effect of higher temperatures was a change of the reactance, mainly due to the modification of the sound celerity inside the cavities.

2.2 Description of the setup

In order to study the coupling between thermal and acoustic effects, measurements are carried out with grazing flow and various acoustic and thermal conditions in the ONERA B2A grazing flow facility.

2.2.1 The B2A bench

The B2A test bench is made of a stainless steel tube with a square section of side $a = 50$ mm and a total length of about 4 m. A mean flow of bulk Mach number M_b up to 0.5 can be provided, its temperature can be regulated from room temperature up to 570 K.

The test section is 0.2 m-long and equipped with two opposing silica windows for optical access. An exponential quasi-anechoic outlet terminates the duct, leading to a reflection coefficient smaller than 0.2 for frequencies higher than 500 Hz. The surface of the test liner forms a 150 mm-long portion of the lower wall of the flow duct and spans all the duct width (Minotti et al. 2008).

Upstream of the test section, two speakers are used to generate tones (usually a multi-sine signal) at up to 150 dB over a frequency range of 0.3 to 3.5 kHz (i.e. the no-flow cut-off frequency of the duct for plane waves). When a multi-sine source is used, the overall SPL (OASPL) within the duct is much higher (usually 10 dB more) than the SPL at each tone frequency.

Sixteen microphone sockets in the upper wall of the test section are used for acoustic measurements and impedance eduction. The upper wall with the microphone sockets is removable and can be replaced by a cover with static pressure

Table 1: Geometric characteristics of the samples

Sample	ϕ	Porosity (POA)	δ	Inner cavity height	Total height
SDOF-1	1.5 mm	15%	1 mm	48 mm	50 mm
SDOF-2	1.5 mm	15%	8 mm	41 mm	50 mm

sockets or a window for infrared measurements. Silica windows on both sides allow near-wall optical measurements (LDV or PIV).

In the duct, the flow is in a fully-developed turbulent state, with axial velocity fluctuations on the centerline being a few percent of the bulk velocity U_b (Léon et al. 2019). The parameter used for the regulation of the grazing flow is its mass flow rate $q_m = \rho M_b c_0 S$ (in grams per second), where $M_b = \frac{U_b}{c_0}$ is the bulk Mach number, $S = a^2$ is the duct cross-section, and c_0 is the sound speed in the duct.

Table 2 shows the different flow rates used in this study and the corresponding bulk Mach numbers at room temperature.

Table 2: Flow rates used and Mach numbers associated

q_m	M_b ($T_{flow} = 20°C$)
50	0.048
100	0.097
150	0.145
200	0.194
260	0.251

2.2.2 Design of the test cell

The thermal configuration chosen for this study is defined by the sign of the temperature difference ΔT between the flow and the bottom of the liner. The bottom wall of the liner is heated and the flow, which is regulated at room temperature, acts as a cold thermostat to obtain a positive thermal gradient in the sample.

To ensure this configuration can be obtained in a stable manner, a new test section has been designed. This new section is partly based on the one developed for the study by Méry et al. (2019) and has been optimized for the goals of this study. It is made of steel so that the cell can withstand high temperatures while remaining sealed and without undergoing significant thermal expansion.

The sample holder associated with that test section has been designed for optimum thermal insulation. Indeed, in order to characterize the thermal gradient inside the sample, the exchanges must take place mainly between the upper and lower walls and not on the four side walls. In order to guarantee this insulation, two steel plates covered with ceramic plates and placed along the entire length of the sample have been added on both sides. They rest on a rail created in the lateral wall and are also used to hold the sample in position. The device used to heat the bottom of the liner sample is placed directly under the sample and is also insulated from the lateral walls, as the ceramic plates are taller than the typical liner sample we use.

A sketch of the cross-section of the testing cell and sample holder in the flow direction is presented in figure 3a. The insulating plates are shown in red, they effectively prevent any contact between the sample and the support on both sides.

2.2.3 Thermal setup

The bottom of the sample is heated by two electric resistors with a total output of 200 W. The resistors are screwed under a thin aluminum plate positioned just under the sample. This setup ensures a good heating distribution. In addition, the junction between the aluminum plate and the sample is sealed with thermal paste to ensure a good thermal conductivity.

The heating is regulated by an external system allowing to have a constant given temperature on the bottom of the sample. This system combines a PID controller (Acim Jouanin 48CSP2E) and a solid-state relay (Acim Jouanin RS25480) and works by setting a temperature target and controlling the resistors' power input to adjust to the true temperature measured with a type K thermocouple placed on top of the aluminum plate. The temperature obtained on the bottom of the sample is about 5 to 10 degrees lower than the target temperature obtained on the aluminum plate due to inevitable losses at the junction between the aluminum plate and the sample's backplate in spite of the thermal paste. The heating system can also be operated by directly setting the power input into the resistors (in percentage of the maximum output power of 200 W), allowing to have a constant power under the sample instead of continually adjusting the power to attain a target temperature. This second way is used for the thermal validation of the setup (see Sec.3.2).

2.2.4 Temperature monitoring

Type K thermocouples are used to record backplate and flow temperatures (denoted T_b and T_{flow} respectively), as these define the thermal gap $\Delta T = T_b - T_{flow}$ inside the sample. A third type K thermocouple is placed on the external lateral wall of the sample and measures T_{lat}, allowing

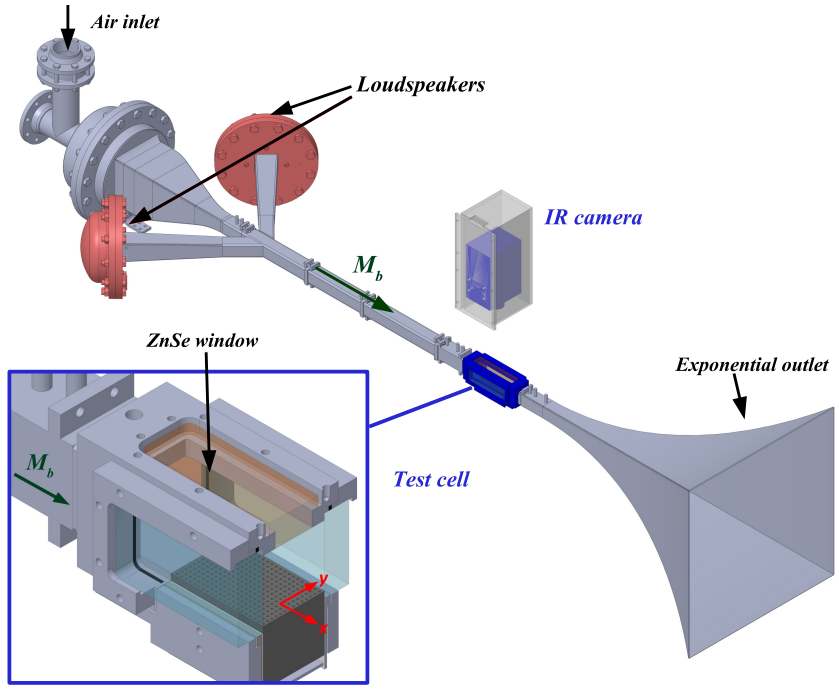

Fig. 1: The B2A bench

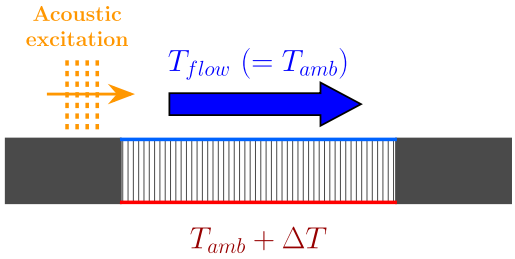

Fig. 2: Thermal configuration studied

to have an insight of the temperature distribution inside the sample. The positions of thermocouples are given in figure 4.

The temperatures of the heating plate (denoted T_{plate}), as well as the input for the PID controller (denoted by T_{set} in figure 4), are considered as parameters external to the setup but are nevertheless carefully monitored to ensure the repeatability of the experiment.

2.3 Preliminary thermal study

A preliminary thermal study was carried out to ensure a correct thermal gradient within the sample (Méry et al. 2019). Let T_b, T_u and T_{flow} be the temperatures of the backplate, the perforated plate and the grazing flow respectively. Let $h = Nu\ \frac{k_{body}}{L_s}$ be the convective heat transfer coefficient between the sample surface and the air flow, where Nu is the Nusselt number, L_s the thickness of the liner, and k_{body} the equivalent thermal conductivity of the liner. Nu is given by Colburn's correlation for a turbulent duct flow:

$$Nu = 0.023 \times Re^{0.8} \times Pr^{1/3}. \tag{1}$$

Consider that the bottom wall of the liner is equipped with a device able to maintain the thermal gap defined by $\Delta T = T_b - T_{flow}$. Solving the 1D heat equation yields :

$$T_u = T_{flow} + \frac{P_d}{h}, \tag{2}$$

$$T_b = T_u + \frac{P_d \times L_s}{k_{body}}, \tag{3}$$

$$P_d = \frac{T_u - T_{flow}}{1/h + L_s/k_{body}}, \tag{4}$$

where P_d is the heat flux density transmitted between the bottom of the liner and the flow through the device and h is the convective transfer coefficient.

The solution to these equations is linked to the Biot number:

$$Bi = \frac{L_s h}{k_{body}} = \frac{T_b - T_u}{T_u - T_{flow}}. \tag{5}$$

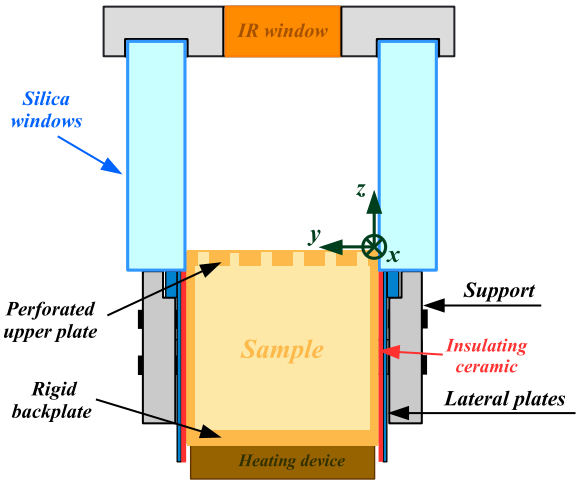

(a) Cross-section of the testing cell (facing downstream)

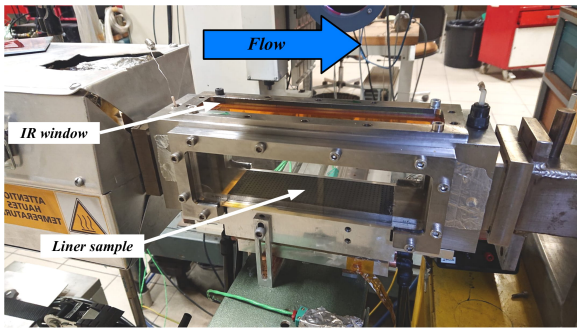

(b) Picture of the test section (the flow and x axis go from left to right)

Fig. 3: Experimental setup for thermal gradient control

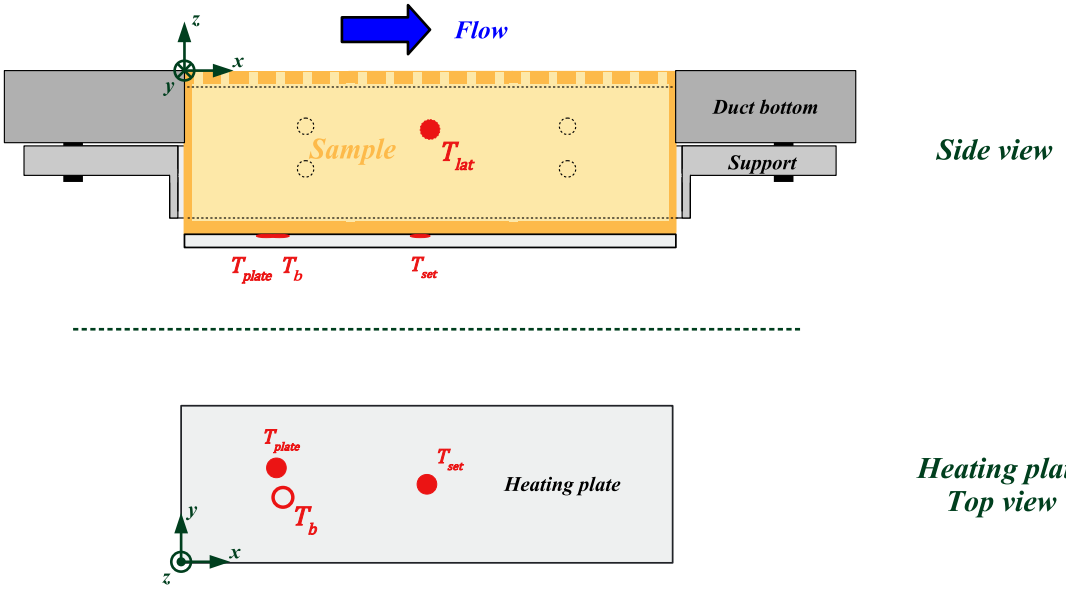

Fig. 4: Positioning of thermocouples in the test section

Indeed, the value of the ratio $\frac{T_b - T_u}{T_u - T_{flow}}$ indicates where the heat transfer occurs: a Biot number larger than one means that there is a significant temperature gradient inside the sample, while a Biot number smaller than 0.1 implies that the heat conduction inside the body is much faster than the heat convection away from its surface, and temperature gradients are negligible inside of it. In the present case, this pre-study gives a theoretical value $Bi = 5$. The corresponding experimental results give $Bi = 2.1$, lower than the theoretical value but remaining within the same order of magnitude (Méry et al. 2019).

In addition to being a useful way of designing the thermal setup, the Biot number is a quite simple way to obtain experimentally the value of h using the values of T_b, T_u and T_{flow} as well as the characteristics of the liner sample L_s and k_{body}.

3 Infrared thermography

The temperature of the perforated plate T_u is obtained by infrared thermography. Infrared (IR) thermography is a method to measure the temperature of a body by measuring the infrared radiation it emits. The technique relies on

a good understanding of the physical phenomena involved and requires carefully controlled experimental conditions. An IR camera and a specific IR window with surface treatment adapted to transmit almost 100% of the incident infrared radiation are used. The IR window is placed in the top wall of the test section, allowing to see from above the perforated sheet of the sample. The camera is a FLIR SC7600 MWIR with a 25mm lens, the window is a ZnSe window specifically made for the B2A bench.

3.1 IR measurement setup

The emitted radiation is a function of the temperature of the material: hotter objects emit a greater intensity of infrared energy. The link between the intensity emitted and the temperature is obtained using the Stefan–Boltzmann formula for a greybody:

$$W = \varepsilon \sigma T^4, \tag{6}$$

where σ is the Stefan-Boltzmann's constant, T is the temperature (in K), and ε is the emissivity of the greybody.

The emissivity of real objects varies with the wavelength ($\varepsilon = \varepsilon(\lambda)$), thus they are not true greybodies. However, for IR thermography measurement only a short range of wavelengths is considered (3-5 μm). In this range, ε can be considered constant.

The measurement is taken at a short distance, allowing to disregard the influence of the atmosphere as its transmittance is very close to 1 (Le Sant et al. 2002; Gaussorgues 1994). The camera is mounted outside of the test section and settled so that the surface of the sample can be fully observed. As the test cell has to remain sealed, it is equipped with a specific ZnSe window: this window is treated on both its faces to transmit almost all the infrared radiation coming from the sample towards the camera.

The intensity observed by the camera is given by:

$$\begin{aligned} W_{meas} = \tau_{window} \left(\varepsilon_{obj} W_{obj} + (1 - \varepsilon_{obj}) W_{env} \right) \\ + (1 - \tau_{window}) W_{window}, \end{aligned} \tag{7}$$

where τ_{window} is the transmittance of the ZnSe window and ε_{obj} is the emissivity of the sample. A calibration is needed to obtain the transmittance of the window. The calibration is done by observing a blackbody of known emissivity and temperature through the window and comparing with a direct observation, to deduce the amount of radiation absorbed by the window. In our case, the window was found to have a transmittance $\tau_{window} = 0.98$.

For the measurement, ε_{obj} needs to be known. This is achieved by coating the surface of our samples with a specific paint of high known emissivity. With all these parameters, the internal calibration of the camera ($W = f(T)$) is able to determine the temperature of the observed surface.

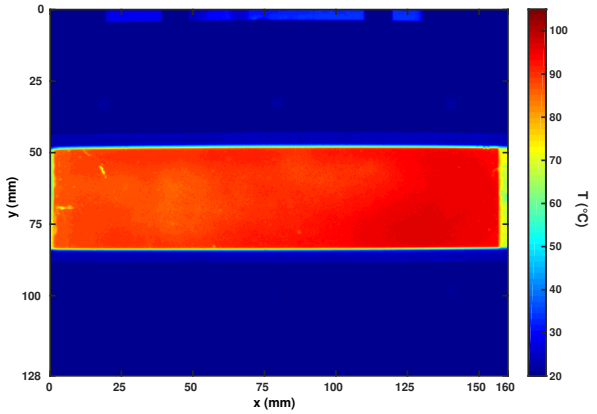

(a) Rigid wall, q_m = 100 g/s, T_{flow} = 20°C, Temperature range 2

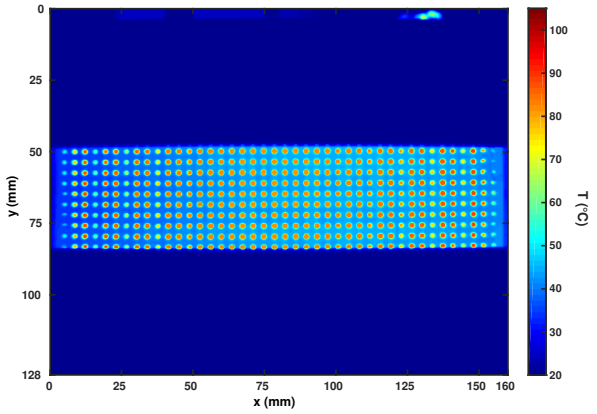

(b) Sample SDOF-1, q_m = 100 g/s, ΔT = +100 K, Temperature range 1

Fig. 5: Examples of raw infrared pictures

Two examples of raw infrared pictures are displayed in figure 5. The raw pictures are 640 pixels wide and 512 pixels high. The spatial resolution is approximately 4 pixels per millimeter. The camera is set up in order to have the area of interest centered in the picture, to minimize the impact of the distortion caused by the lens at the extremities. The camera's internal calibration law is established for several specific temperature ranges. In this work, two distinct calibrations were used: the first one is valid for 15°C < T_u <73°C (range 1), the other one is valid for 67°C < T_u <150°C (range 2). However in most cases, T_u was either low enough or high enough to be able to use only one calibration at a time.

3.2 Validation of the setup

A series of measurements on a rigid wall is conducted to validate the setup. For these measurements, the "sample" is a simple aluminum block with dimensions equal to those of

the liner samples. Even though no significant thermal gradient is expected inside the block due to its high conductivity (k_{al} = 237 W/m/K), thermocouples are placed as detailed in figure 4. In this rigid wall case, the heating device is set to deliver a constant power (expressed as a percentage of its maximum power) instead of a preset temperature, thus the thermocouple giving T_{set} is not used.

Figures 6 and 7 show the infrared thermography results obtained with the rigid wall, with the heating device set at 100% of its capacity. Heat convection effects are well marked: the surface temperature decreases when the flow speed increases due to the increase of the convective heat transfer coefficient h.

The thermal insulation on the sides of the sample that was described in 2.2 seems effective: the temperature is quite homogeneous along the cross-section of the sample, indicating that there are no important losses along the y-direction.

The temperatures recorded by the different thermocouples when thermal equilibrium is reached (i.e. when the temperature of the heating plate and the temperatures measured by all the thermocouples become stable within the ±1 K inherent error margin of the thermocouples) as well as the surface averaged value of T_u measured with IR thermography are listed in Table 3. For all cases, T_{set} is over 130°C. The whole setup appears to be thermally stable, and the thermal gradient inside the rigid block is negligible as the huge majority of thermal transfers occur between the block and the environment, on both faces.

Table 3: Measured temperatures in different places of the setup. Rigid wall, no acoustic excitation.

q_m	T_{flow} (°C)	M_b	T_u (°C)	T_{lat} (°C)	T_b (°C)
50	20	0.048	114	118	122
100	20	0.097	98	101	105
150	20	0.145	88	90	95
200	20	0.194	80	85	90
260	20	0.251	73	78	84

The averaged h coefficient is calculated by plotting the averaged surface temperature against the power density on the bottom of the sample. Using Newton's law, $\frac{1}{h}$ is directly given by the slope of the affine fitting of the obtained curve, plotted in figure 8. Table 4 gives the values of h in the rigid wall setup. When P_d = 0 kW/m^2, the obtained temperature is equal to T_{aw} and not T_{flow}.

The Biot number Bi associated with that setup is obtained using Eq.5. The Biot number is around 0.1, which confirms that the plain metal sample is thermally thin: most of the thermal gradient occurs between the sample and the flow.

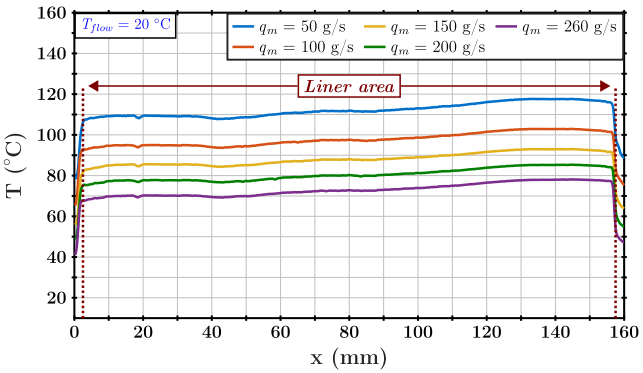

Fig. 6: Surface temperature T_u for several flow speeds (rigid wall, without acoustic excitation). Streamwise profile (spanwise averaged).

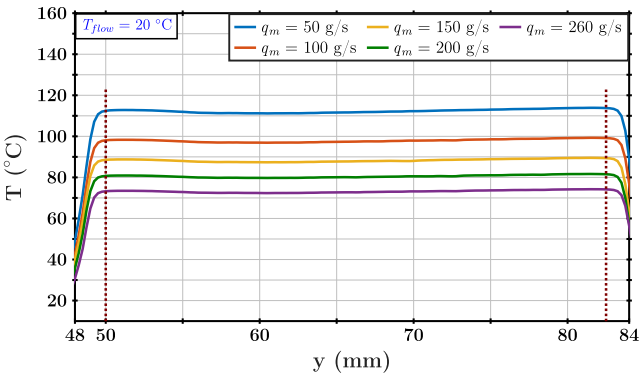

Fig. 7: Surface temperature T_u for several flow speeds (rigid wall, without acoustic excitation). Cross-sectional profile (streamwise averaged).

Table 4: Values of h and T_{aw}

q_m	M_b (T_{flow} = 20°C)	h (W.m^{-2}.K^{-1})	Bi	T_{aw} (°C)
50	0.048	311	0.065	27.3
100	0.097	388	0.081	25
150	0.145	468	0.099	24.8
200	0.194	518	0.109	23

4 Measurements on SDOF liners

For each thermal configuration and each sample, the objective is to assess the turbulent and acoustic effects by comparing the surface temperatures of the liner with and without acoustic excitation.

4.1 Effect of the grazing flow

The effect of the grazing flow is assessed by measuring the liner's surface temperature without any acoustic excitation and with an established thermal gradient at several flow speeds. In this case, the temperature difference between the

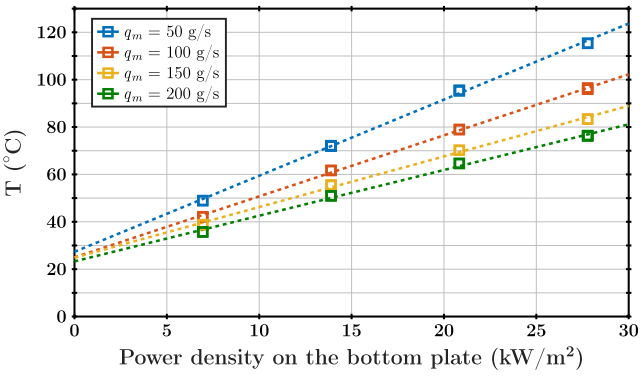

Fig. 8: T_u (surface averaged) as a function of P_d, rigid wall.

top and the bottom of the sample is equal to +100 K. Figures 9a and 9b show the temperature along the liner surface for all the considered flow speeds. The averaged profiles are obtained taking profiles in the flow direction, in a non-perforated zone and near the center of the section to minimize boundary effects.

The heat convection effect is well marked, as the liner's surface temperature decreases when the flow rate q_m increases: this is due to the increase of the convective heat transfer coefficient h as the increasing flow dissipates more the heat at the surface of the sample. This is confirmed by thermocouple measurements on the lateral wall of the sample, as seen in figures 10a and 10b: the "inside" temperature T_{lat} follows the variations of the surface temperature T_u (measured with IR thermography), indicating that the air moves inside the liners' cavities.

The behaviors of both samples appear very similar, given that their surfaces are geometrically identical. The small and regular oscillations of the surface temperature streamwise profiles are due to the perforations (even if the profile is taken in a non-perforated zone). The surface temperature profile appears to have a curved repartition with a maximum temperature in the final quarter of the liner. This asymetric shape can be explained by the thermal discontinuity between the test section and the liner. Such a discontinuity implies a local increase of the convective heat transfer coefficient followed by a decrease down to an asymptotic convective heat transfer coefficient value. Further investigations should be conducted to assess this effect. Downstream, again a decrease of the surface temperature is observed due to imperfection of the setup: this decrease is due to thermal losses due to conductivity effect between the liner and the test section. This effect is also expected upstream but the local increase of the convective heat transfer overwhelms this effect.

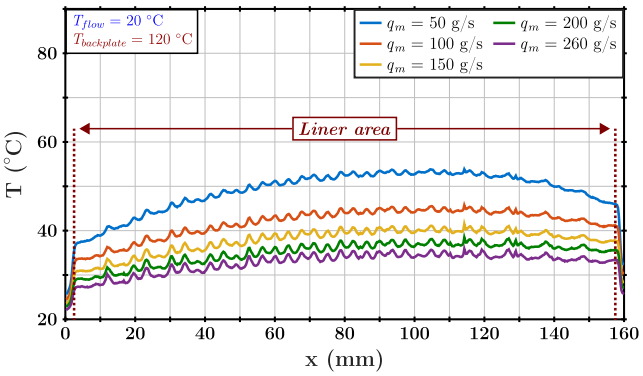

(a) Sample SDOF-1

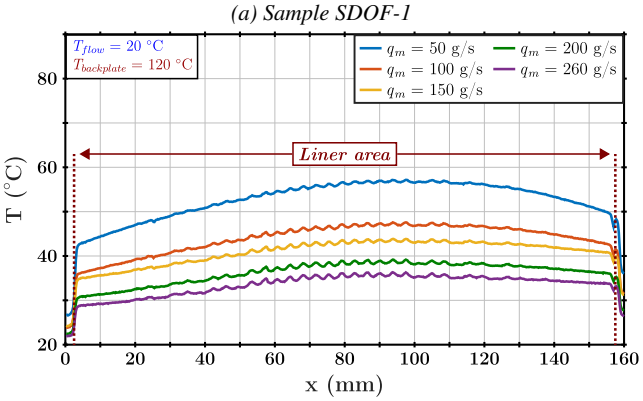

(b) Sample SDOF-2

Fig. 9: Surface temperature for ΔT = +100 K for several flow speeds, without acoustic excitation. Streamwise profile (spanwise averaged)

4.2 Effect of the acoustic level

The study on the acoustic effects is done on both samples as they are expected to exhibit different behaviors due to their characteristics. A two-microphone method (Åbom 1989) is used in the B2A duct to control the sound pressure level (SPL) incident into the sample (i.e., the sound pressure level of the downstream wave). This wave sorting approach is applied in order to extract and thus control the downstream wave SPL in presence of flow (under uniform flow assumption) (Primus et al. 2013; Roncen et al. 2019; Lafont et al. 2020). Mono-sine or multi-sine acoustic excitation can be used. The multi-sine is made of 12 pure tones ranging from 504 Hz to 2824 Hz and of equal incident SPL, while the mono-sine is only a single pure tone (its frequency is chosen among the 12). In the following, the incident SPL is always indicated per tone, meaning that a 130 dB/tone excitation has in fact an overall SPL (OASPL) of around 140 dB. Multi-sine excitations are used to study global behaviors at low and medium SPLs while mono-sine excitations are used for studying the behavior at higher SPLs and at specific frequencies, for example near the liner's resonance.

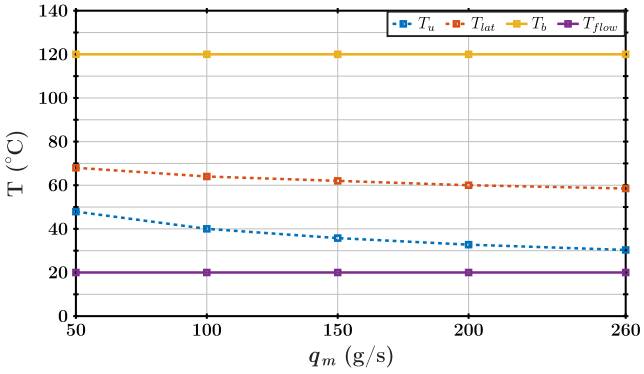

(a) Sample SDOF-1

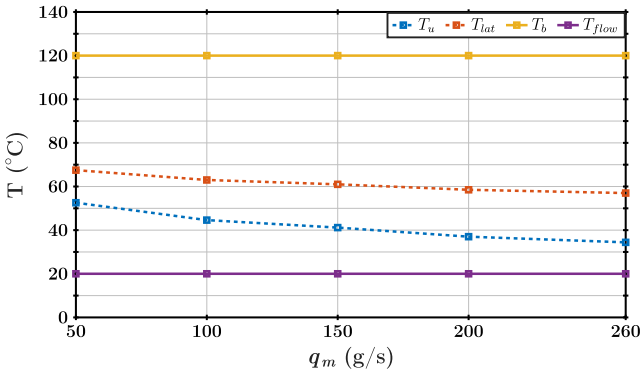

(b) Sample SDOF-2

Fig. 10: Measured temperatures in different places of the setup, for various flow speeds. ΔT = +100 K, no acoustic excitation

Table 5 lists the 12 frequencies used for the excitations. The frequencies in bold are those chosen for the different mono-sine excitations.

Figure 11 illustrates the decrease of the acoustic level over the liner, as measured by microphones on the wall opposite the liner. The measured SPL is a total SPL and is thus higher than the 140 dB set for the incident downstream wave at the beginning of the lined zone. The liner's absorption effect appears clearly.

4.2.1 Global effect

The first step is to study the global effect of the acoustic waves. This is done by using a multi-sine excitation and varying the incident SPL from 115 dB to 130 dB. The temperatures measured at each level are then compared to the temperature measured without the acoustic excitation. Results from this measurement on liner SDOF-1 are shown in Figure 12. The thermal difference between backplate and flow is fixed at 100 K. The surface temperature decreases when an acoustic excitation is applied, indicating that the thermal exchanges at the wall are modified. When the SPL increases, reaching the limits of the non-linear range of the

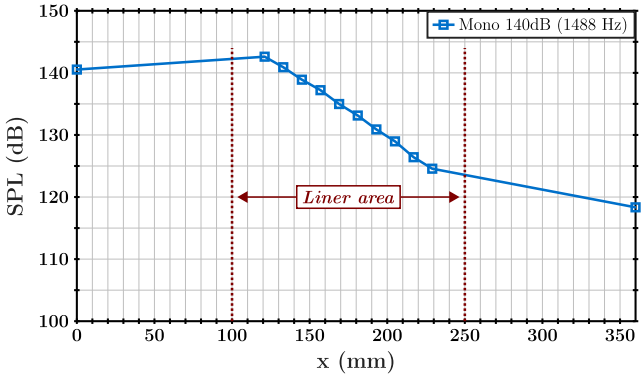

Fig. 11: Total SPL over the liner (opposite wall microphone measurements). Sample SDOF-1, q_m = 50 g/s, ΔT=+100 K, Single tone excitation (140 dB incident SPL)

sample, the effect on the temperature increases too. The effect is clearly linked to the air convection near the surface, which is increased with the acoustic waves.

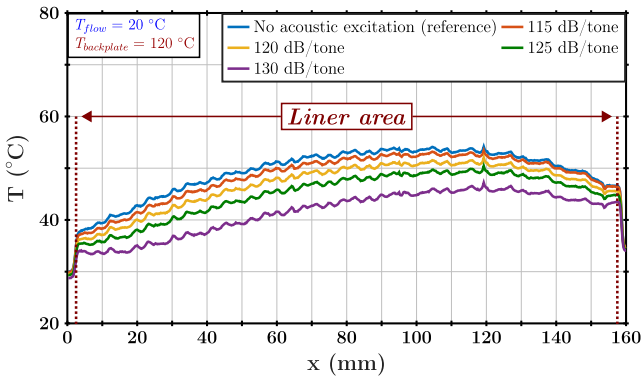

Fig. 12: Sample SDOF-1, q_m = 50 g/s, ΔT=+100 K, different sound excitations (115 to 130 dB), streamwise profile.

Moreover, the lateral thermocouple indicates that the temperature distribution inside the samples themselves is also modified when the acoustic excitation is present , as seen in figure 13.

In order to simplify the study, we chose to describe the effects at the liner surface using the Biot number *Bi* (see Eq.5) instead of the temperature, as it allows easier comparisons between thermal configurations thanks to its link to the convective heat transfer coefficient.

In the case of multi-sine excitations, the coupling between acoustics and thermal effects appears to be even on the whole liner surface. It can therefore be described using an averaged Biot number calculated over the complete surface. As shown in figure 14, when the acoustic excitation is present , the averaged Biot number increases: as all other boundary conditions remain unchanged, this means that the heat convection increases at the surface of the sam-

Table 5: Frequencies used. Bold numbers indicate frequencies used for mono-sine excitations

Frequencies (Hz)											
504	616	760	**992**	1112	1240	**1488**	1736	1992	2248	2488	2824

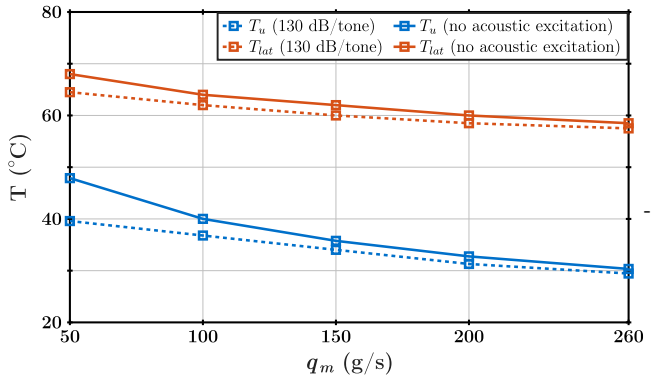

(a) Sample SDOF-1

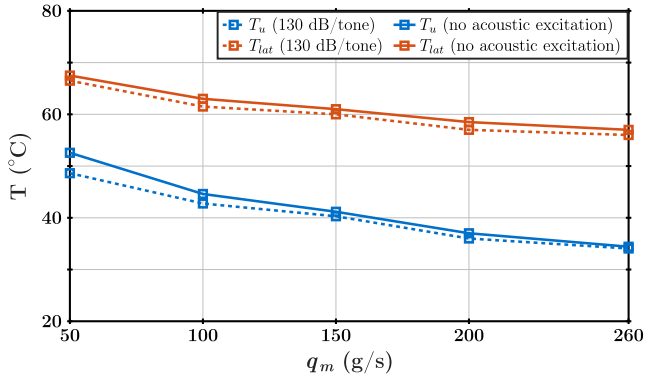

(b) Sample SDOF-2

Fig. 13: Influence of acoustic excitation on measured temperatures at the surface (T_u, IR thermography) and on the side of the samples (T_{lat}, thermocouple measurement), various flow speeds, ΔT=+100 K. Solid lines without acoustic excitation, dashed lines with acoustic excitation set at 130 dB/tone

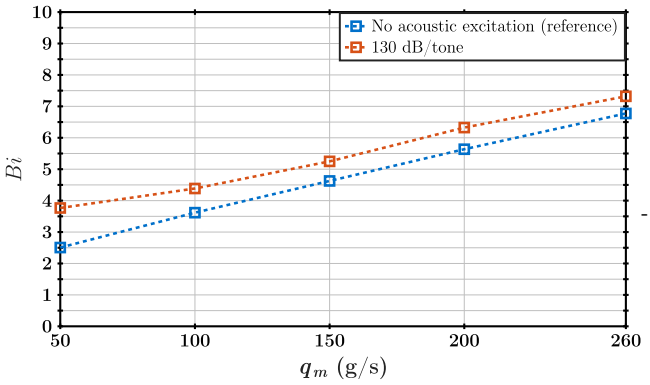

(a) Sample SDOF-1

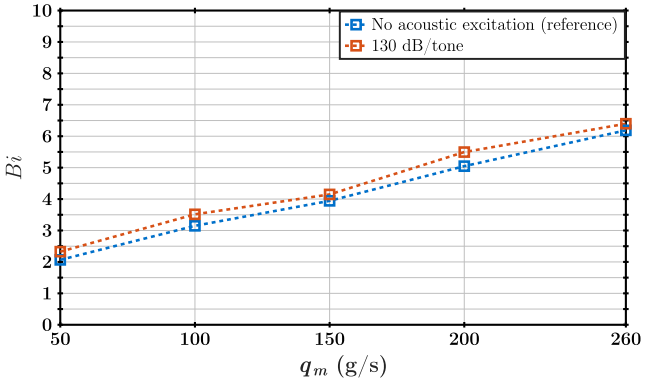

(b) Sample SDOF-2

Fig. 14: Biot number (averaged over the sample surface) as a function of q_m, SPL=130 dB/tone, ΔT=+100 K

ple. Hence, the temperature at the surface changes and gets closer to the flow temperature.

The distinct acoustic behaviors of the two samples can be seen by comparing the heat convection change caused by the acoustic level: the Biot number increases more with the SDOF-1 than with the SDOF-2 at the same flow conditions. The non-linear behavior of sample SDOF-1 seems to be an important parameter in the coupling between thermal and acoustic effects, since this coupling does not appear as much on the linear sample SDOF-2.

4.2.2 Local effect

To ensure that the temperature modification observed is indeed linked to the acoustic behavior of liners, a series of measurements using single tones is necessary. The frequencies are chosen close to the resonance of each sample.

On sample SDOF-1, the resonance is around 1500 Hz and the frequency for the excitation is set at 1488 Hz. For sample SDOF-2, the excitation frequency is set at 992 Hz (the resonance is around 1 kHz). The incident SPL is set at 140 dB (the OASPL is thus equal to the OASPL of the multi-sine excitation presented in the previous section). As with multi-sine excitations, the temperature is modified. However, this time the effect is local instead of global: the modification is important at the beginning of the sample but the temperature gradually returns to its reference level at the end of the liner. The corresponding Biot numbers (spanwise

averaged) are plotted in figures 15 and 16 for both samples. The Biot number obtained with multi-sine excitations at 130 dB/tone are added for comparison. The local convection modification is visible on sample SDOF-1: the local Biot Number *Bi* is higher than with the multitone excitation of same OASPL at the start of the liner, but then decreases to finally reach the reference value at the end of the sample. Sample SDOF-2 also exhibits this behavior, with a lower intensity.

The coupling between thermal and acoustic effects is thus more intense near the resonance of the sample, but also more local. This is mainly due to the absorption of the liner near the resonance: as the sound wave travels over the liner's surface, it is progressively dissipated and its SPL decreases (as seen in figure 11), which decreases in turn the additional convective effect. This is not visible on multi-sine excitations as the frequencies that are less absorbed (i.e. the frequencies which are far from the resonance) counterbalance this absorption effect.

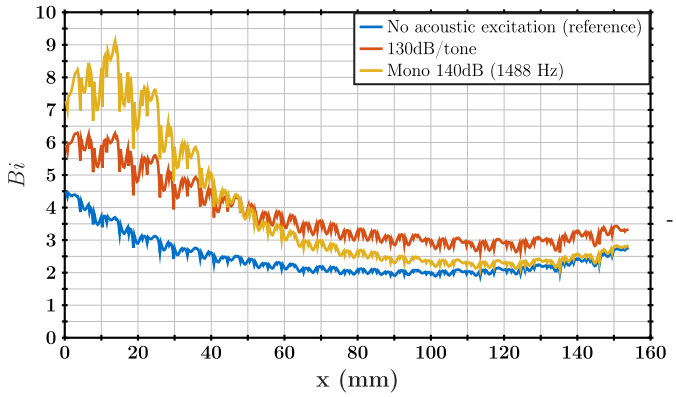

(a) Sample SDOF-1

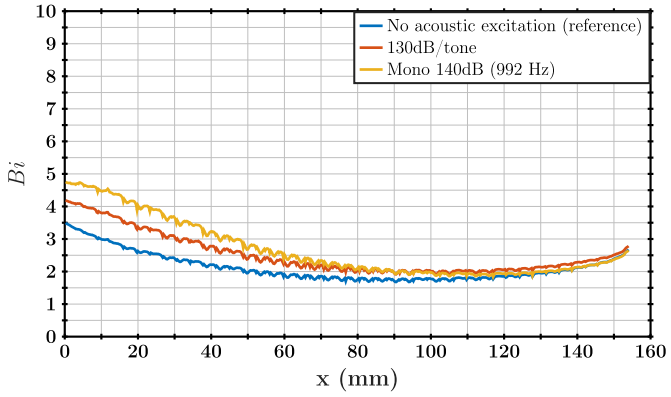

(b) Sample SDOF-2

Fig. 15: Streamwise Biot number (spanwise averaged), ΔT=+100 K, q_m = 50 g/s

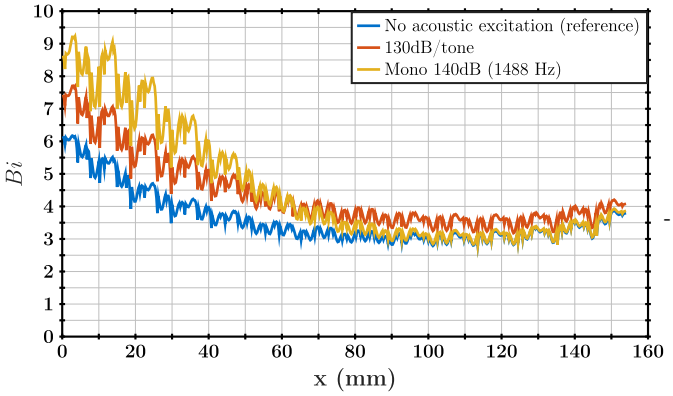

(a) Sample SDOF-1

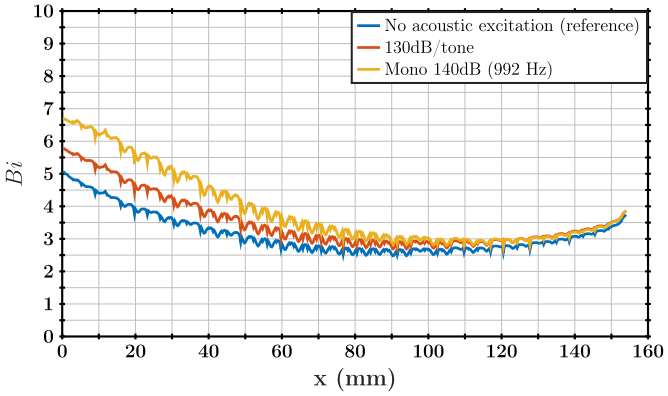

(b) Sample SDOF-2

Fig. 16: Streamwise Biot number (spanwise averaged), ΔT=+100 K, q_m = 100 g/s

4.2.3 Link with the acoustic impedance

In the present section, the microphone measurements will be used as input for the eduction process on both liners at their resonance frequency (i.e. 1488 Hz for SDOF-1 and 992 Hz for SDOF-2) in presence of the thermal gradient. A link between the impedance of the liner and the heat convection effect can then be made, using the experimental impedance eduction technique developed in Lafont et al. (2020). The effect of the SPL on the liner resistance is presented as an additive term.

The model on the resistance term can be written as:

$$r = r_L + r_{NL}, \tag{8}$$

where r_L is the value of the resistance in the linear regime regarding the SPL and includes the grazing flow effect, and r_{NL} is the additional term directly linked to the non-linear SPL effect. To catch the impedance variation due to high SPL with our eduction procedure with shear grazing flow, the idea is to educe the nonlinear part of the resistance while taking into account the decrease of the SPL along the lined region. In the streamwise direction, the impedance of the

liner is no more constant and reads:

$$\zeta(x) = r_L + j\chi + D(x - L_\tau) \times \mathbb{1}_{0<x<L_\tau}(x), \tag{9}$$

where D is the slope coefficient and L_τ represents the length of the part of the liner over which the resistance is expected to change due to the SPL effect: when $x > L_\tau$, only the constant term r_L remains (see Lafont et al. (2020) for more details). The non-linear effect due to the SPL effect can be highlighted with the present impedance formulation. This formulation makes sense only when the grazing flow is low, as there is a competition between the SPL and the grazing flow effect which also induces an increase of the resistance r. For a given flow rate that depends of the considered liner, the grazing flow effect overwhelms the SPL non linear effect. Further details on this eduction formulation can be found in Lafont et al. (2020). Figure 17 presents eduction results compared to thermal results. It presents the resistance obtained with the conventional constant impedance eduction method (Primus et al. (2013); Roncen et al. (2019)) and the new formulation with a variable resistance eduction method (Lafont et al. (2020)) superimposed to the Bi results along the liner, for a frequency close to the resonance and at a low flow rate, on both samples. The new eduction formulation catches well the increase of resistance due to the SPL effect, particularly on sample SDOF-1. The thermal results are coherent with this resistance evolution: they highlight a localized effect which is confirmed by the impedance eduction process. The intensity of the localized thermal effect is higher on the SDOF-1 than on the SDOF-2, and the variable formulation is also able to catch that difference. The increase of the Biot value is thus highly linked to the variation of the acoustic resistance of the liner: when a liner is highly responsive to SPL effect compared to other effects such as the grazing flow, the convective heat transfer coefficient is increased. It suggests that the vortex shedding at the aperture of the liner holes is increased so that the thermal exchanges are also increased. This behavior has already been shown in Léon et al. (2017), where the modification of the log-law velocity profile at the wall vicinity due to SPL effect were seen as a uniform transpiration effect. The present study seems to confirm this kind of analogy since the thermal exchanges are locally increased by the high SPL near the resonance of the liners.

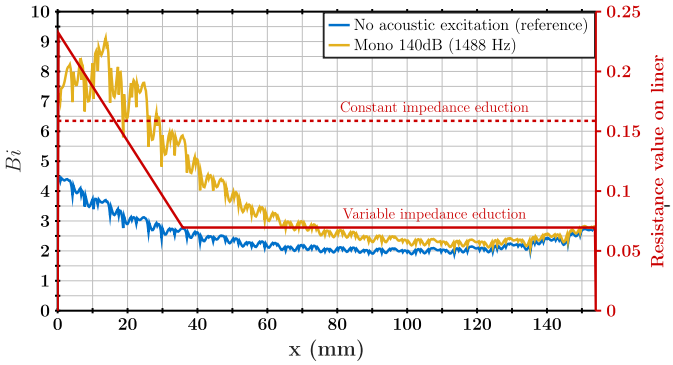

(a) Sample SDOF-1

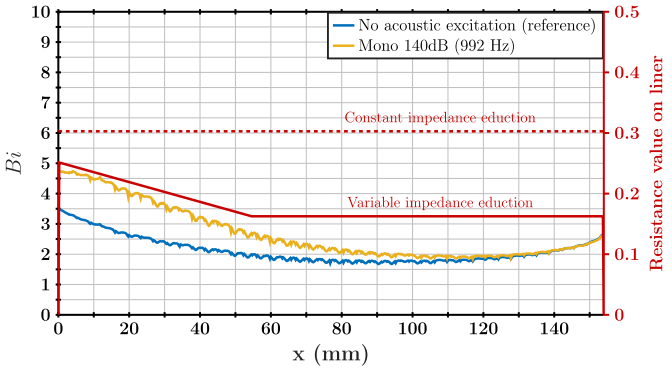

(b) Sample SDOF-2

Fig. 17: Streamwise Biot number, spanwise averaged, and resistance r educed with a monosine excitation at 140 dB near the sample resonance. ΔT=+100 K, q_m = 50 g/s

5 Conclusions

Infrared thermography was used to study the behavior of simple SDOF liners under the influence of grazing flow, high SPL and thermal gradient. A strong coupling between high acoustic levels and temperature has been found when the acoustic frequency is close to the resonance, whether the liner is linear or non-linear with respect to SPL. On the non-linear liner, the coupling also appears strongly near the resonance when the overall acoustic level exceeds the non-linearity threshold. The coupling exists whether the flow is heated or not, but almost vanishes at high flow speeds due to the grazing flow effect being stronger than the acoustic level effect at these flow rates.

The coupling is related to an increase of the heat convection at the surface of the liner. Hence, the Biot number Bi was used to describe it accurately. Around the resonance, the evolution of Bi along the liner (in the direction of the flow) is similar to the evolution of the liner's resistance educed using the impedance eduction technique developed in Lafont et al. (2020). Indeed, both decrease gradually as the incident acoustic wave is absorbed along the liner, highlighting the existence of a link between the resistance value and the heat convection effect. For Nacelle liner design, when considering low velocity flow and non-linear liners, heat transfers are modified by the acoustic environment and must therefore be taken into account particularly for de-icing issues. For higher flow velocity or linear liners, the coupling is weaker and the flow speed is the key driver for the heat transfer. Thanks to this methodology, several type of liners (different perforated sheet features or Double Degree of Freedom

(DDOF) liners) could be assessed in order to derive new models for thermal behavior.

Acknowledgements The work presented in this paper has been funded by Région Occitanie. The authors thank Delphine Sebbane and Nicolas Fasano for designing and helping with the experimental setup, and Thomas Batmalle for helping during the infrared measurements. Estelle Piot and Rémi Roncen are warmly acknowledged for their helpful insight on the impedance eduction part.

References

Åbom M (1989) Modal decomposition in ducts based on transfer function measurements between microphone pairs. Journal of Sound and Vibration 135(1):95–114, DOI 10.1016/0022-460X(89)90757-8

Bodén H, Åbom M (1986) Influence of errors on the two-microphone method for measuring acoustic properties in ducts. The Journal of the Acoustical Society of America 79(2):541–549, DOI 10.1121/1.393542

Busse-Gerstengarbe S, Richter C, Thiele FH, Lahiri C, Enghardt L, Roehle I, Ferrante P, Scofano A (2012) Impedance eduction based on microphone measurements of liners under grazing flow conditions. AIAA Journal 50(4):867–879, DOI 10.2514/1.J051232, https://doi.org/10.2514/1.J051232

Chandrasekharan V, Sheplak M, Cattafesta L (2006) Experimental study of acoustic impedance of mems-based micro-perforated liners. vol 1, DOI 10.2514/6.2006-2401

Chung JY, Blaser DA (1980) Transfer function method of measuring in-duct acoustic properties. i. theory. The Journal of the Acoustical Society of America 68(3):907–913, DOI 10.1121/1.384778, https://doi.org/10.1121/1.384778

Elnady T, Bodén H (2004) An inverse analytical method for extracting liner impedance from pressure measurements. In: 10th AIAA/CEAS Aeroacoustics Conference, vol 1, DOI 10.2514/6.2004-2836

Elnady T, Bodén H, Kontio T (2004) Impedance of SDOF perforated liners at high temperatures. In: 10th AIAA/CEAS Aeroacoustics Conference, p 2842

Elnady T, Bodén H, Elhadidi B (2009) Validation of an inverse semi-analytical technique to educe liner impedance. AIAA Journal 47(12):2836–2844, DOI 10.2514/1.41647

Gaussorgues G (1994) Infrared Thermography. Springer Science, Netherlands, DOI 10.1007/978-94-011-0711-2

Guess A (1975) Calculation of perforated plate liner parameters from specified acoustic resistance and reactance. Journal of Sound and Vibration 40(1):119–137, DOI 10.1016/S0022-460X(75)80234-3, URL http://www.sciencedirect.com/science/article/pii/S0022460X75802343

Hersh A, Walker B, Celano J (2003) Helmholtz resonator impedance model, part 1: Nonlinear behavior. AIAA journal 41(5):795–808, DOI 10.2514/2.2041

Howerton B, Jones M (2017) A conventional liner acoustic/drag interaction benchmark database. DOI 10.2514/6.2017-4190

Jasinski C, Corke T (0) Mechanism for increased viscous drag over porous sheet acoustic liners. AIAA Journal 0(0):1–12, DOI 10.2514/1.J059039, https://doi.org/10.2514/1.J059039

Jing X, Peng S, Sun X (2008) A straightforward method for wall impedance eduction in a flow duct. The Journal of the Acoustical Society of America 124(1):227–234, DOI 10.1121/1.2932256

Jones M G, Watson W R, Parrott T L (2005) Benchmark data for evaluation of aeroacoustic propagation codes with grazing flow. In: Proceedings of the 11th AIAA/CEAS Aeroacoustics Conference, AIAA-2005-2853, Monterey, California, vol 2853, p 2005, DOI 10.2514/6.2005-2853

Kirby R, Cummings A (1998) The impedance of perforated plates subjected to grazing gas flow and backed by porous media. J Sound Vib 217(4):619–636, DOI 10.1006/jsvi.1998.1811

Lafont V, Méry F, Roncen R, Simon F, Piot E (2020) Liner impedance eduction under shear grazing flow at a high sound pressure level. AIAA Journal 58(3):1107–1117, DOI 10.2514/1.J058756, https://doi.org/10.2514/1.J058756

Lavieille M, Simon F, Micheli F (2006) Measurement of acoustic quantity fields in duct flow by Laser Doppler Velocimetry. In: Proceedings of the 12th AIAA/CEAS Aeroacoustics Conference, AIAA-2006-2550, Cambridge, Massachusetts, DOI 10.2514/6.2006-2550

Le Sant Y, Marchand M, Millan P, Fontaine J (2002) An overview of infrared thermography techniques used in large wind tunnels. Aerospace Science and Technology 6(5):355 – 366, DOI 10.1016/S1270-9638(02)01172-0, URL http://www.sciencedirect.com/science/article/pii/S1270963802011720

Léon O, Piot E, Sebbane D, Simon F (2017) Measurement of acoustic velocity components in a turbulent flow using ldv and high-repetition rate piv. Experiments in Fluids 58(6):72, DOI 10.1007/s00348-017-2348-4

Léon O, Méry F, Piot E, Conte C (2019) Near-wall aerodynamic response of an acoustic liner to harmonic excitation with grazing flow. Experiments in Fluids 60(9):144, DOI 10.1007/s00348-019-2791-5

Minotti A, Simon F, Gantié F (2008) Characterization of an acoustic liner by means of laser doppler velocimetry in a subsonic flow. Aerospace Science and Technology 12(5):398–407, DOI 10.1016/j.ast.2007.09.007, URL http://www.sciencedirect.com/science/article/pii/S1270963807001150

Motsinger R, Kraft R (1991) Design and performance of duct acoustic treatment. Aeroacoustics of Flight Vehicles: Theory and Practice Volume 2: Noise Control

Méry F, Piot E, Sebbane D, Reulet P, Simon F, Carazo Méndez A (2019) Experimental assessment of the effect of temperature gradient across an aeroacoustic liner. Journal of Aircraft 56(5):1809–1821, DOI 10.2514/1.C035157, https://doi.org/10.2514/1.C035157

Primus J, Piot E, Simon F (2013) An adjoint-based method for liner impedance eduction: Validation and numerical investigation. Journal of Sound and Vibration 332(1):58–75, DOI 10.1016/j.jsv.2012.07.051, URL http://www.sciencedirect.com/science/article/pii/S0022460X12006268

Rademaker ER, van der Wal HM, Geurts EG (2009) Hot-stream in-situ acoustic impedance measurements on various air-filled cavity and porous liners. ICVS16

Rienstra SW, Singh DK (2018) Nonlinear asymptotic impedance model for a helmholtz resonator of finite depth. AIAA Journal 56(5):1792–1802, DOI 10.2514/1.J055882

Roncen R, Méry F, Piot E, Simon F (2019) Statistical inference method for liner impedance eduction with a shear grazing flow. AIAA Journal 57(3):1055–1065, DOI 10.2514/1.J057559

Watson W, Jones M, Parrott T (1999) Validation of an impedance eduction method in flow. AIAA journal 37(7):818–824

Watson WR, Jones MG, Tanner SE, Parrott TL (1996) Validation of a numerical method for extracting liner impedance. AIAA journal 34(3):548–554

Zhang Q, Bodony DJ (2016) Numerical investigation of a honeycomb liner grazed by laminar and turbulent boundary layers. Journal of Fluid Mechanics 792:936–980, DOI 10.1017/jfm.2016.79

Conflict of interest

The authors declare that they have no conflict of interest.